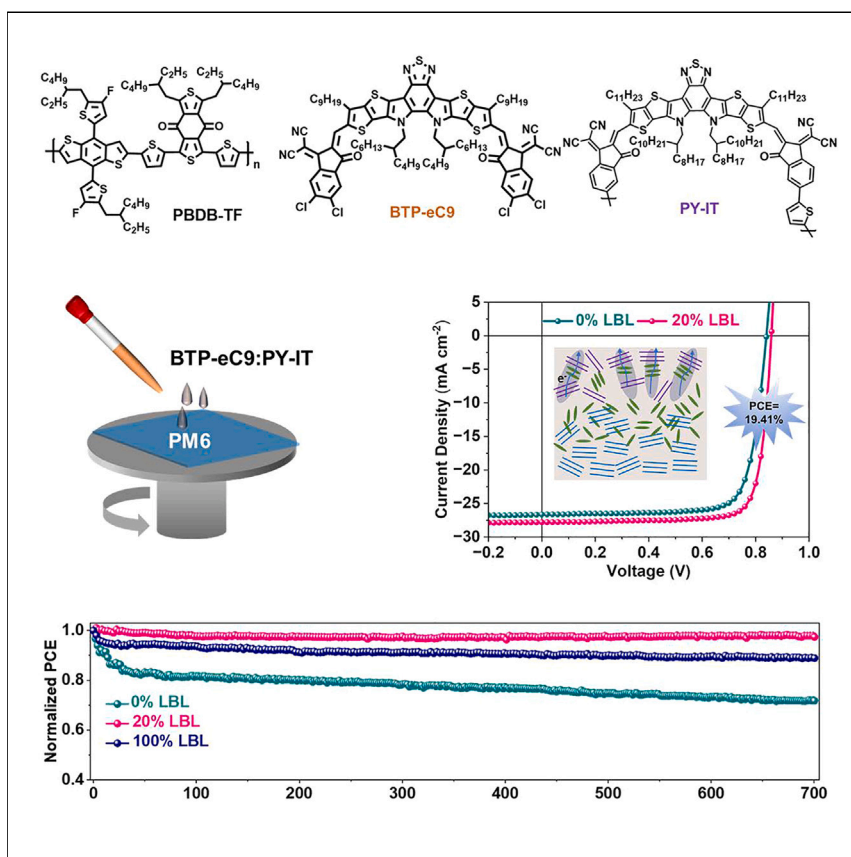## Article

Achieving 19.4% organic solar cell via an *in situ* formation of p-i-n structure with built-in interpenetrating network

Ying Zhang, Wanyuan Deng, Christopher E. Petoukhoff, ..., Xinhui Lu, Yang Yang, Gang Li

yangy@ucla.edu (Y.Y.)
gang.w.li@polyu.edu.hk (G.L.)

Highlights

The GPT-LBL strategy strengthens the p-i-n structure by aggregation tuning of acceptors

A highly efficient GPT-LBL device with a PCE of 19.41% (certified 19.0%) was achieved

The GPT-LBL strategy enhances the operational stability of OSCs

We developed a guest polymer-tailored LBL (GPT-LBL) strategy to successfully build the desired p-i-n OSC configuration, where the third guest polymer molecule PY-IT can fine-tailor the aggregation behaviors in the upper layer and thus the interdiffusion of donor and acceptor. This reinforced built-in p-i-n microstructure with better domain connectivity enables enhanced charge transport and minimized energy loss. As a result, the GPT-LBL-based device exhibits a device efficiency of 19.41% (certified as 19.0%) with excellent operational stability.

Joule

CellPress

Article

Achieving 19.4% organic solar cell via an *in situ* formation of p-i-n structure with built-in interpenetrating network

Ying Zhang,[1,6] Wanyuan Deng,[2] Christopher E. Petoukhoff,[3] Xinxin Xia,[4] Yongwen Lang,[1] Hao Xia,[1] Hua Tang,[3] Hrisheekesh Thachoth Chandran,[1] Sudhi Mahadevan,[5] Kuan Liu,[1] Patrick W.K. Fong,[1] Yongmin Luo,[7] Jiaying Wu,[7] Sai-Wing Tsang,[5] Frédéric Laquai,[3] Hongbin Wu,[2] Xinhui Lu,[4] Yang Yang,[6,*] and Gang Li[1,8,*]

SUMMARY

Vibrant research has demonstrated that the layer-by-layer (LBL) approach can achieve a preferable vertical microstructure; however, the lack of precise control over vertical composition and molecular organization remains. Herein, we demonstrated a guest polymer-tailored LBL (GPT-LBL) strategy to achieve the p-i-n microstructure constructed by *in situ* monitoring pre-aggregation behaviors of non-fullerene acceptors. This superior structure with built-in interpenetrating networks alleviates the trap density states and the energy loss, improves hole transfer dynamics, and balances the charge transport, thus maximizing open-circuit voltage (V_{OC}), short-circuit current density (J_{SC}), and fill factor (FF) simultaneously. Consequently, a highly efficient GPT-LBL organic solar cell (OSC) with a power conversion efficiency (PCE) of 19.41% (certified 19.0%) was achieved. Noticeably, the large-area (1.03 cm^2) device for GPT-LBL OSCs yields a satisfactory PCE of 17.52% in open-air blade coating, which is one of the best values in green-solvent-processed OSCs. The insights for p-i-n structure will give implications for the device engineering and photo physics understanding, offering an effective way to enable efficient, stable, and scalable OSCs.

INTRODUCTION

Organic solar cells (OSCs) have enjoyed tremendous research attention owing to their unique characteristics, such as low weight, transparency, mechanical flexibility, and roll-to-roll production.[1–6] It is worth mentioning that the emergence of state-of-the-art small molecular non-fullerene acceptors (NFAs) has pushed the power conversion efficiencies (PCEs) surpassing 19% in single-junction bulk heterojunction (BHJ) OSCs.[7–13] Despite recent progress, the performance of BHJ OSCs is still limited by non-ideal charge transport as well as severe electronic trap state density due to the nature of the electronic structure of organic semiconductors, which can be relieved via suitable nanostructure. In BHJ OSCs, it is formed by self-organization of material crystallization and phase separation in BHJ donor (D) and acceptor (A).[14,15] Traditionally, the dominant BHJ structure creates numerous D-A heterojunctions located at the bulk regions randomly for exciton dissociation,[16] but in the meantime exists the risk of undesirable vertical phase separation, which may suffer from charge recombination. Recent studies have claimed that p-i-n configuration or graded BHJ (G-BHJ) would afford superior vertical phase-separated domains: where As are

CONTEXT & SCALE

Organic solar cells (OSCs) have seen great progress in power conversion efficiencies (PCEs) recently. However, morphology tuning of the active layer remains challenging toward 20% mark. Layer-by-layer (LBL) approach is a newer way to tune morphology and achieve phase separation vertically. Herein, we construct a guest polymer-tailored LBL (GPT-LBL) strategy refining the p-i-n configuration, where a third polymeric guest PY-IT is utilized to *in situ* manipulate the pre-aggregation behaviors of acceptors. The GPT-LBL-based device exhibits enhanced charge transport and reduced energy loss. As a result, the optimal GPT-LBL OSC shows a high PCE of 19.41% (certified 19.0%) with an excellent FF of 81.3%, which is the record-certified LBL single-junction OSC. Impressively, the GPT-LBL-based device exhibited good scalability and operational stability. This work provides a novel approach to developing high-efficiency, large-area, and stable OSCs, accelerating the industrial development of OSCs.

enriched at the cathode side, Ds are enriched at the anode side and D/A-mixed regions are sandwiched between them, thus forming a more ideal nanomorphology that benefits charge transport without sacrificing exciton dissociation efficiencies.[17–20] Such vertical component stratification can be more readily realized via layer-by-layer (LBL) or bilayer processing, in which the D and A can be optimized independently.[21,22] More importantly, it has been demonstrated that LBL approach can widen solvent-processing window and suppress the scaling lag of OSC module efficiency, showing excellent compatibility with large-area coating, better thick devices, and the potential to realize scaled-up manufacturing.[18,23–25] Generally, these advantages have resulted in significant interest in the LBL strategy and its potential for large-scale and stable OSC manufacturing.

Bearing in mind that the BHJ and LBL processes build nanomorphology in a fundamentally different way. The one-step blend-cast BHJ is a complex process, which is a toughly controllable process resulting from multiple effects of thermodynamics, kinetics, D-A intermolecular interactions (e.g., miscibility), etc. In addition, the optimal morphology in BHJ devices is usually a metastable state and will further move to a thermodynamic equilibrium state to form excessive phase aggregation, leading to deduction of lifetime and performance of OSCs.[26,27] On the contrary, LBL process relies on swelling of the underlying D layer by the solvent of the A solution to drive quasi-solid state interdiffusion of the two materials, accompanied by the crystallization of the upper material in the meantime.[28,29] Hence, the eventual p-i-n morphology would be kinetically facilitated by these two competitive processes,[22] which can be controlled via solvent engineering, like the solvent screening for the upper layer,[30] solvent selection for the bottom D,[31] the crystallinity of bottom material,[29,32] etc. Therefore, finely balancing the molecular interdiffusion and crystallization (e.g., molecular aggregation in the upper layer) in the LBL process might be the effective pathway for achieving a p-i-n stratification of the two components for favorable hole and electron transport. It was well studied that the third component can act as a crystallization regulator to manipulate film morphology, which has boosted great success in ternary-based BHJ OSCs.[33,34] Based on this view, rational selection of the third component in the upper layer can offer the possibility of co-optimizing the molecular self-aggregation and interdiffusion in the LBL approach, thus achieving more preferred vertical phase separation. As we all know, small molecules with limited molecular size are more easily diffused into the underlying layer, leading to too much intermixed heterojunction between two layers. Polymer As with entangled chains are the potential candidates for strengthening the stratification due to their larger molecular size, which limits the movement downward into the swelled spaces within the bottom layer. In addition, the doping of macromolecule can act as the morphology locker to inhibit molecular diffusion by formation of robust network fibers, which would be beneficial to improve the long-term stability of p-i-n devices.[35,36]

Herein, we proposed an effective and feasible guest polymer-tailored LBL (GPT-LBL) strategy to constituent the p-i-n configuration toward high-performance LBL-OSCs via incorporating the guest (polymeric Acceptor Poly[(2,2′((2Z,2′Z)-((12,13-bis(2-octyldodecyl)-3,9-diundecyl-12,13-dihydro[1,2,5] thiadiazolo [3,4e]thieno[200,300:40,50] thieno[20,30:4,5]pyrrolo[3,2-g]thieno[20,30:4,5] thieno[3,2-b]indole-2,10-diyl)bis(methanylylidene))bis(5-methyl-3-oxo-2,3-dihydro-1H-indene-2,1diylidene)) dimalononitrile-co-2,5-thiophene (PY-IT) into the host poly[(2,6-(4,8-bis(5-(2-ethylhexyl)-4-fluorothiophen-2-yl) benzo[1,2-b:4,5-b']dithiophene))-co-(1,3-di(5-thiophene-2-yl)-5,7-bis (2-ethylhexyl)benzo[1,2-c:4,5-c']dithiophene-4,8-dione(PM6)/2,2′-[[12,13-Bis(2-butyloctyl)-12,13-dihydro-3,9-dinonylbisthieno[2″,3″:4′,5′]thieno[2′,3′:4,5]pyrrolo[3,2-e:2′,3′-g][2,1,3]

[1]Department of Electrical and Electronic Engineering, Research Institute for Smart Energy (RISE), Photonic Research Institute (PRI), The Hong Kong Polytechnic University, Hong Kong 999077, China

[2]State Key Laboratory of Luminescent Materials and Devices, Institute of Polymer Optoelectronic Materials and Devices, South China University of Technology, Guangzhou 510640, China

[3]KAUST Solar Center, Physical Sciences and Engineering Division (PSE), Material Science and Engineering Program (MSE), King Abdullah University of Science and Technology (KAUST), Thuwal, Jeddah 23955-6900, Kingdom of Saudi Arabia

[4]Department of Physics, The Chinese University of Hong Kong, New Territories, Hong Kong 999077, China

[5]Department of Materials Science and Engineering, Center of Super-Diamond and Advanced Films (COSDAF), City University of Hong Kong, Hong Kong 999077, China

[6]Department of Materials Science and Engineering, University of California, Los Angeles, CA 90025, USA

[7]The Hong Kong University of Science and Technology, Function Hub, Advanced Materials Thrust, Nansha 511400, Guangzhou, China

[8]Lead contact

*Correspondence: yangy@ucla.edu (Y.Y.), gang.w.li@polyu.edu.hk (G.L.)

https://doi.org/10.1016/j.joule.2023.12.009
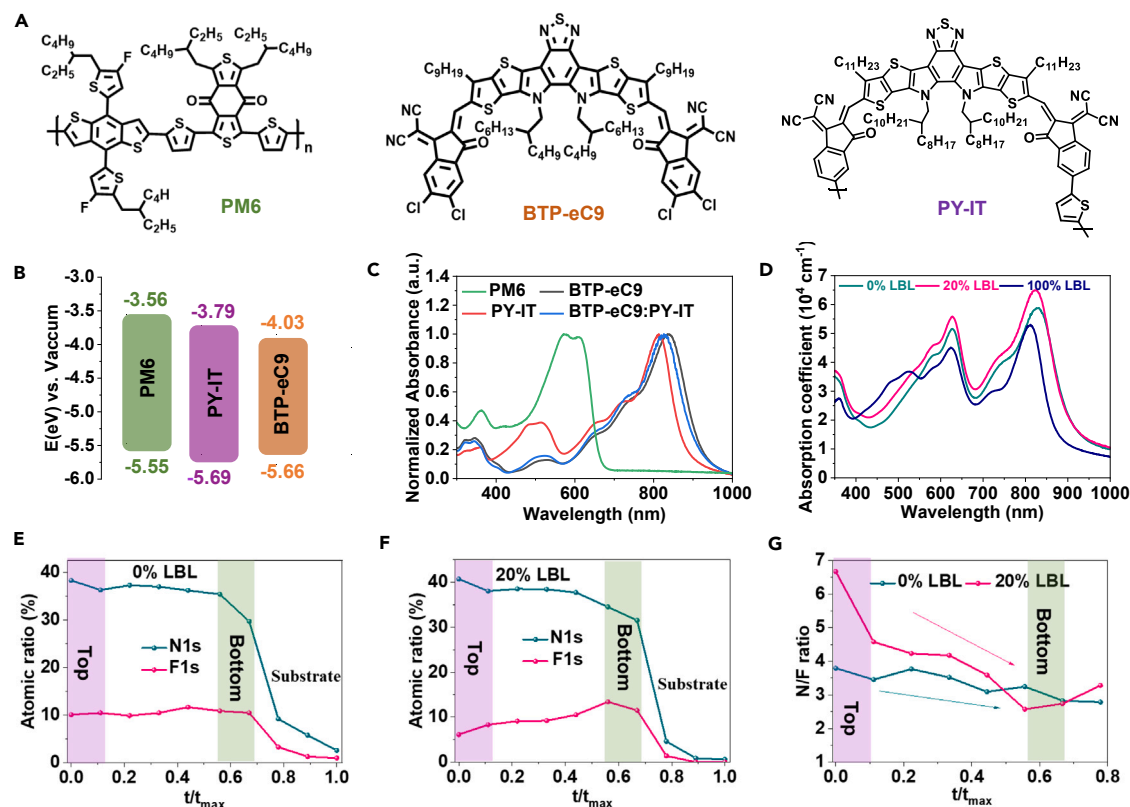
Joule
Article

CellPress

Figure 1. The molecular structures and optoelectrical properties of materials and vertical composition distribution in the LBL-based films

(A) Chemical structures of the donor and acceptors.

(B) Energy levels alignment of materials used in this work.

(C) Normalized UV-vis spectra of neat donor and acceptor(s)-based films.

(D) Absorption coefficients of 0% LBL, 20% LBL, and 100% LBL films.

(E and F) Selected atomic fractions of (E) 0% LBL film and (F) 20% LBL film as a function of sputtering time.

(G) D/A variations as a function of sputtering time for 0% and 20% LBL blend films.

benzothiadiazole-2,10-diyl]bis[methylidyne(5,6-chloro-3-oxo-1H-indene-2,1(3H)-diylidene)]]bis[propanedinitrile] (BTP-eC9) OSC system[20] processed by environmentally friendly solvent o-xylene (XY). Our *in situ* and *ex situ* morphological characterizations offer a clear microstructural landscape—more pronounced p-i-n formation constructed by rationally regulating the pre-aggregation kinetics of the upper layer (BTP-eC9 mixed with guest PY-IT). The carrier dynamics and energy loss analysis elucidate that the improved hole transfer (HT) dynamics and the inhibited trap states contribute to the simultaneously improved V_{OC}nsm these advantages, a highly efficient and eco-friendly GPT-LBL-OSCs with a PCE of 19.41% (certified 19.0%) with an excellent FF of 0.813 was achieved, More importantly, during transferring from spin coating to blade coating, small-area (0.036 cm^2) and large-area (1.03 cm^2) GPT-LBL-OSCs with outstanding PCEs of 18.45% and 17.52% via open-air green solvent printing were successfully demonstrated, which are among the highest PCEs reported for large-area state-of-the-art OSCs, reducing the gap during the lab-to-fab transfer. Remarkably, robust light stability is also obtained, in which the 20% LBL device maintains about 96% of its initial PCE after 700 h of operation at the maximum power point (MPP) under continuous light illumination.

RESULTS AND DISCUSSION

Figures 1A and 1B show the chemical structures and the energy levels of PM6, BTP-eC9, and PY-IT. Electrochemical cyclic voltammetry (CV) measurements were

performed to determine the energy levels of PM6, BTP-eC9, and PY-IT. The corresponding CV curves are shown in Figure S1. Figure 1C displays the normalized UV-vis absorption spectra of PM6, BTP-eC9, PY-IT, and mixed A films. The three materials show complementary absorption and suitable energy level alignment. 0% LBL film denotes control PM6/BTP-eC9, the 20% LBL using GPT-LBL strategy is the film in which 20% of PY-IT is added in the mixed As in the upper layer (see device fabrication in the supplemental information), whereas 100% LBL film denotes PM6/PY-IT. We measured the absorption coefficients for different LBL blends (Figure 1D). The corresponding measured absorbance spectra are provided in Figure S2. 20% LBL film using XY as the solvent exhibits a higher absorption coefficient than the 0% LBL film in both the D and A absorption regions. The reason for such different absorption coefficients in 0% LBL and 20% LBL blends may be associated with the varied blend morphology or molecular packing, which will be revealed in the following characterizations.[24,37] Before fabricating the devices, we first studied the vertical component distribution of different blends. First of all, we performed the contact angle (CA) tests on water (H_2O) and ethylene glycol (EG) to distinguish composition on the film surface, and the results are shown in Figure S3. Based on CA results, we can estimate the surface energies (γ) according to Wu's model,[38] which are summarized in Table S1. The surface energies of neat PM6, BTP-eC9, and PY-IT are 26.9, 33.8, and 31.5 mN m^{-1}, respectively, suggesting that the enriched As on the top surface would increase surface energy values.[39] Both the 0% LBL film and 20% LBL film show larger surface energies, indicating that the As have very high content on the top surface. Then, depth profiling X-ray photoelectron spectroscopy (DP-XPS) was performed to further confirm the distribution of the components in the vertical direction including the top surface, the bulk, and the bottom (Figures 1E–1G). The samples were prepared on the silicon substrates. In these films, since only PM6 contains fluorine (F), BTP-eC9 contains the characteristic element chloride (Cl), and both BTP-eC9 and PY-IT contain nitrogen (N), three materials contain oxygen (O), we attribute the F1s spectral line to PM6, N1s spectral line to the As, O1s spectral line to three components, and N/F could reflect the degree of As penetration in the D domains. The detailed atomic fractions are listed in Table S2. It was found that the contents of N element at the top surface in these two films are 38.3% and 40.7%, respectively, F contents are 10.1% and 6.1%, respectively. The higher N content and lower F content at the top surface in the 20% LBL film represent more As gathered at the top (close to the cathode). With the increase in detection depth from top to bottom, the ratio of N/F decreases gradually from 3.8 to 2.8 for 0% LBL film, whereas 20% LBL film displays obviously sharper reduction from 6.7 to 2.7. This result suggests that the addition of PY-IT would restrain the penetration of As into the D layer, leaving a purer A domain at the top surface and a more compact D matrix at the bottom (close to the anode of the device). To support the DP-XPS results, we also conducted the time-of-flight secondary ion mass spectrometry (TOF-SIMS) measurements (Figure S4). The F^- and CN^- signals represent the D and the A, respectively. For 20% LBL film, it was obvious that the signal intensity of CN^- declined continuously from the top to the bottom. Meanwhile, the signal intensity of F^- was much stronger in the bottom part than those in the top part. This result demonstrated that the more pronounced p-i-n structure with A-enrichment at the top and D-enrichment at the bottom was formed, which is well consistent with the DP-XPS results. Both DP-XPS and TOF-SIMS measurements show that the GPT-LBL strategy can effectively promote active layer stratification vertically.

Photovoltaic performances

To investigate the photovoltaic performances, we fabricated OSCs via a conventional device structure of indium tin oxide (ITO)/poly(3,4-ethylenedioxythiophene):polystyrene
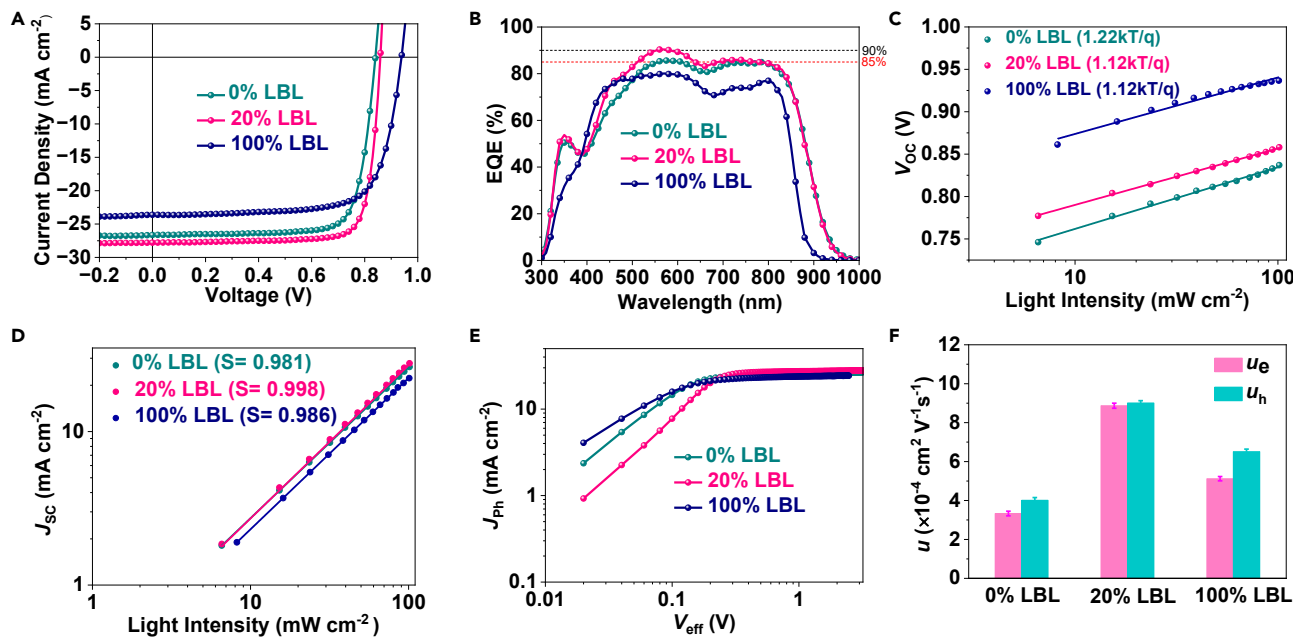
Figure 2. Device performances and charge dynamics

(A) *J-V* curves of 0% LBL, 20% LBL, and 100% LBL devices.

(B) EQE curves of the corresponding devices with different weight ratios of PY-IT.

(C) Light intensity-dependent V_{OC} for optimized 0%, 20%, and 100% LBL devices.

(D) Light intensity-dependent J_{SC} for optimized 0%, 20%, and 100% LBL devices.

(E) Photocurrent density (J_{ph}) plotted versus effective bias for optimized 0%, 20%, and 100% LBL devices.

(F) Histogram of hole and electron mobilities for optimized 0%, 20%, and 100% LBL devices determined by SCLC measurements (error bar is defined as the standard deviation).

sulfonate (PEDOT:PSS)/active layer (BHJ/LBL)/PFN-Br/Ag. More fabrication details can be found in the supplemental information. As presented in the current density-voltage (*J-V*) curves (Figure 2A) and the detailed photovoltaic parameters summarized in Table 1, the optimal device based on 0% LBL delivered a PCE of 17.53%, with a V_{OC} of 0.840 V, a J_{SC} of 26.65 mA cm^{-2}, and an FF of 0.783. The best-performing 20% LBL device (GPT-LBL device) gave a maximum PCE of 19.41% with simultaneously improved V_{OC} (0.859 V), J_{SC} (27.79 mA cm^{-2}), and FF (0.813). To the best of our knowledge, 19.41% is among the best efficiencies for single-junction LBL-OSCs processed via both halogenated and non-halogenated solvents, as summarized in Table S3. It is noted that the best cell was sent to the Enli Tech Optoelectronic Calibration Lab, Taiwan, for measurement, and a certified PCE of 19.0% was achieved (Figure S5), which is among the highest certified efficiencies for LBL-based devices. The certificate of accreditation is provided in Figure S6. The spin-coated 100% LBL film processed from XY solution was grainy after

Table 1. Device performances of LBL OSCs processed by XY with different PY-IT contents in mixed acceptors under the illumination of an AM 1.5G solar simulator, 100 mW cm^{-2}

Devices	V_{OC} (V)	J_{SC} (mA cm^{-2})	FF	PCE$_{max}$ (PCE$_{avg}$)[a] (%)	$J_{calc.}$[b]
0% LBL	0.840 (0.839 ± 0.002)	26.65 (26.54 ± 0.13)	0.783 (0.778 ± 0.010)	17.53 (17.41 ± 0.10)	26.08
20% LBL (GPT-LBL)	0.859 (0.857 ± 0.003)	27.79 (27.54 ± 0.23)	0.813 (0.809 ± 0.003)	19.41 (19.15 ± 0.20)	27.05
20% LBL[c] (GPT-LBL)	0.858	27.82	0.796	19.0	–
100% LBL[d]	0.939 (0.938 ± 0.003)	23.62 (23.51 ± 0.13)	0.731 (0.719 ± 0.009)	16.21 (15.87 ± 0.20)	22.96

[a]Average PCE values calculated from independent 10 devices.

[b]J_{sc} values obtained from the EQE curves.

[c]Certified result from the Enli Tech Optoelectronic Calibration Lab, Accreditation Criteria: ISO/IEC 17025:2017.

[d]100% LBL devices are fabricated via CF solvents.

CellPress

Joule
Article

depositing the upper XY solvent, which is primarily due to the limited solubility and thus strong pre-aggregation of PY-IT in XY solvent, consequently leading to a poor device. The reason may be that the XY is a weak solvent for PY-IT, and it would be self-aggregated first and enriched at the top, thus hardly diffusing into the bottom.[28] The 100% LBL device gave a poor PCE of 12.83% (Figure S7; Table S4); thus, we changed the processing solvent to chloroform (CF). The resulting 100% LBL cell processed by CF exhibited a PCE of 16.21% with a V_{OC} of 0.939 V, a J_{SC} of 23.62 mA cm^{-2}, and an FF of 0.731. We also fabricated their corresponding BHJ counterparts for comparison, whose *J-V* curves and relevant device parameters are displayed in Figure S8 and Table S5. It was found that all three parameters, especially V_{OC} (0.858 V) and FF (0.792) were similarly enhanced for the ternary BHJ devices (20%), surpassing those (0.839 V and 0.778) of 0% BHJ counterpart, confirming that PY-IT is a valid third component. Specifically, the 20% BHJ device exhibited a bit lower PCE of 18.19% with a lower J_{SC} (26.78 mA cm^{-2}) and lower FF (0.792) than those (27.79 mA cm^{-2}, 0.813) of 20% LBL solar cell. Likewise, a 100% BHJ device whose PCE is 15.62% with a V_{OC} of 0.938 V, a J_{SC} of 23.16 mA cm^{-2}, and an FF of 0.719 shows inferior performance to a 100% LBL device. The photovoltaic parameters of PM6:BTP-eC9:PY-IT-based BHJ-type and LBL-type OSCs with varied weight ratios of PY-IT in the A mixture are provided in Table S6. We found that LBL-OSCs all show higher FFs and PCEs than BHJ counterparts. These results emphasize that LBL processing could induce better vertical morphology because this approach itself is the natural main origin of vertical stratification.[23] To further demonstrate the general applicability of the GPT-LBL approach, we further employed two representative material systems, PM6/BO-4Cl and D18/L8-BO, for comparison. Detailed fabrication processes can be found in the supplemental information. The *J-V* curves for solar cells prepared with and without PY-IT are illustrated in Figure S9, and their corresponding device parameters are listed in Table S7. Ternary LBL-based devices, PM6/BO-4Cl:PY-IT and D18/L8-BO:PY-IT, exhibited PCEs of 18.34% and 18.77%, respectively, surpassing the PCEs of their binary counterparts (16.86% and 17.47%), and both with clearly higher V_{OC}. These results clearly highlight the general applicability of the GPT-LBL strategy in enhancing the photovoltaic performance of OSCs. Notably, the optimized 20% LBL cell demonstrates high photon utilization efficiency, with external quantum efficiency (EQE) values exceeding 90% in the range of D region (500–600 nm) and 85% over a range of A region 700–800 nm), as shown in Figure 2B. Given that LBL-type OSCs are more promising to realize highly efficient OSCs, we focus on the underlying working mechanisms behind the V_{OC}, J_{SC}, and FF improvements in LBL-based solar cells.

Charge carrier dynamics

To gain more insights into the significant differences in the photovoltaic performance among these devices, we also probed their charge dynamic process including the dissociation, transport, and recombination. The dependence of J_{SC} and V_{OC} on light power (P_{light}) was tested to study the charge recombination in both control LBL and ternary LBL devices. The slope of nkT/q in the function of $V_{OC} \propto nkT/q \ln P$ (k is the Boltzmann constant, q is the elementary charge, and T is the temperature) is related to monomolecular recombination (trap-assisted recombination). Extracted from Figure 2C, the fitted n values of 0% LBL, 20% LBL, and 100% LBL devices are 1.22, 1.12, and 1.12, respectively. Moreover, the exponential factor S in the power law relationship of $J_{SC} \propto P^s$ can be used to estimate the bimolecular recombination loss. As shown in Figure 2D, the calculated S value for the optimal 20% LBL device is approaching unity (0.998), larger than that of 0% LBL device (0.981), indicative of the weaker bimolecular recombination loss under short-circuit conditions. These results suggest that the charge recombination losses (monomolecular and bimolecular recombination) can be effectively alleviated after introducing PY-IT into PM6/BTP-eC9 blend.

Joule
Article

To further investigate the exciton dissociation and charge collection mechanism in the active layers, the photocurrent density (J_{ph}) as a function of effective voltage (V_{eff}) was measured, as plotted in Figure 2E. The ratio of J_{ph}/J_{sat} (the saturation J_{ph}) under the short-circuit condition relates to exciton dissociation efficiency (η_{diss}), and the charge collection efficiency (η_{coll}) is evaluated by the ratio of J_{ph}/J_{sat} at the maximal power output point. The η_{diss}/η_{coll} values are estimated to be 99.4%/91.9%, 99.8%/92.8%, and 97.0%/85.3% for the optimal 0% LBL, 20% LBL, and 100% LBL devices, respectively, as listed in Table S8. The improved η_{diss} and η_{coll} for the optimized 20% LBL device agree with the enhanced J_{SC} and FF.

To examine the improvement of FF in 20% LBL-based devices, we evaluated the charge transport properties by using space-charge-limited current region (SCLC) measurements, as shown in Figure S10 and Table S9. The hole mobility (μ_h) and electron mobility (μ_e) extracted from the SCLC method (Figure 2F) both exhibited the enhanced trend with the incorporation of PY-IT: the μ_h increased from 4.01 × 10^{-4} to 9.00 × 10^{-4} cm^2 V^{-1} s^{-1}, and the μ_e improved from 3.33 × 10^{-4} to 8.87 × 10^{-4} cm^2 V^{-1} s^{-1}, respectively. In addition, the highest and more balanced charge transport (μ_h/μ_e of 1.01) was observed in the optimal 20% LBL devices, which is consistent with the improvement of FF. Photoinduced charger-carrier extraction by linearly increasing voltage (photo-CELIV) measurements was also conducted to obtain the mobilities of the faster carrier components.[40] As Figure S11 shows, we tested the photovoltaic transient current of the three devices at the same delay time. The calculated mobilities were 2.51 × 10^{-4}, 4.63 × 10^{-4}, and 3.59 × 10^{-4} cm^2 V^{-1} s^{-1} for 0% LBL, 20% LBL, and 100% LBL devices, respectively, which are consistent with the results obtained from the SCLC method. We can conclude that the doping of PY-IT leads to higher mobility and balanced charge transport, which could reduce the bimolecular and trap-assisted recombination.

The exciton dissociation behavior is further detected via photoluminescence (PL) measurements of the PM6 neat film and relevant LBL films with different PY-IT contents (Figure S12). The main emission peak of PM6 at 670 nm is quenched in both 0% and 100% binary LBL films. Of particular note, the loading of PY-IT does not suppress the D/A interfaces for exciton dissociation and even further quenches the emission intensity, meaning more efficient charge transfer (CT) between D and A for the 20% LBL blend, thus leading to an enhanced J_{SC}. This might be correlated with the suitable nanostructure that is formed by p-i-n phase separation, which will be discussed in the morphology part.

Exciton diffusion and photophysical analysis

Transient absorption (TA) spectroscopy measurements were performed to investigate the exciton generation and CT kinetics in the LBL blends (Figure 3). Here, we focus on the HT dynamics, since ultrafast energy transfer efficiently funnels excitons from Ds to As in the active layer (Figure 1B), such that these blends achieve close-to-unity charge generation efficiency.[41] As such, an excitation wavelength of 750 nm was used to selectively excite the As without exciting the D in both LBL and BHJ blends. Neat PM6 (excited at 580 nm) had a photobleach (PB) signal at ~580 nm and a very pronounced photoinduced absorption (PIA) signal around 1035 nm (Figure S13), whereas neat PY-IT, neat BTP-eC9, and the A binary blend exhibited PB signals at ~840–860 nm and PIA signals at ~920–930 nm. In the LBL and BHJ blends, the A PB and PIA signals were observed instantaneously after photoexcitation, whereas the PB and PIA for PM6 grew in intensity with increasing pump-probe delay times (Figures 3 and S14). The rising PIA signal of the PM6 at 1,035 nm was chosen to monitor the HT dynamics (Figure 3E), as it was spectrally distinct from the signals of
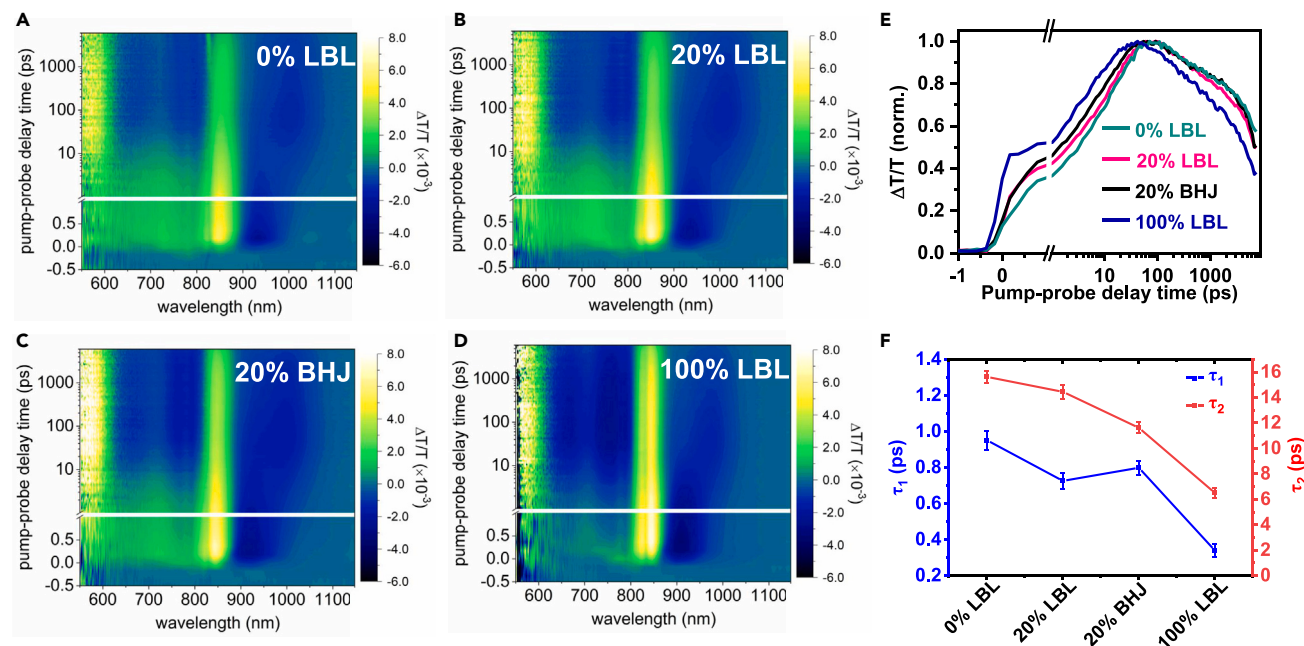
Figure 3. TA images and the corresponding decay dynamics

(A–D) Contour plots of transient absorption spectra of (A) 0% LBL, (B) 20% LBL, (C) 20% BHJ, and (D) 100% LBL blend films under 750 nm excitation.

(E) Picosecond-nanosecond kinetics of the four blended films at a probe wavelength of 1,035 nm, showing the hole transfer process.

(F) Comparisons of τ_1 and τ_2 of different blends (the error bar is from the standard error of curve fitting).

the As and had a greater signal-to-noise ratio than PM6's PB signal. The rising signal from PM6 was fit with a biexponential function, where the fast component was attributed to an ultrafast HT process at the D/A interface (τ_1), and the slow component was attributed to a diffusion-mediated process prior to charge dissociation, controlled by D/A domain size and aggregation (τ_2).[10] The HT process in the four blends (0% LBL, 20% LBL, 20% BHJ, and 100% LBL) showed τ_1 of ~0.95, ~0.73, ~0.80, and ~0.34 ps and τ_2 of 15.62, 14.44, 11.62, and 6.50 ps, respectively (Figure 3F), and their relative contributions are summarized in Table S10. The weight-averaged HT rates for each of the blends were 9.42, 8.10, 6.09, and 3.28 ps, respectively (Table S10), which shows that greater incorporation of PY-IT reduced the exciton diffusion time to the D/A interface and subsequently reduced the HT rate. This indicates that the mixed D-A interfaces and pure domains are synergistically optimized and thus give rise to improved FF and J_{SC}.

Energy loss and deep trap states analysis

In addition, the higher V_{OC} is also an important factor that contributes to the high-efficiency devices. To verify the underlying mechanism of the V_{OC} improvement in the optimal devices, Fourier-transform photocurrent spectroscopy (FTPS) and electroluminescence (EL) measurements were performed to quantitatively analyze the photon energy losses (E_{loss}), as shown in Figures 4A–4C. According to the detailed balance theory, the E_{loss} of a photovoltaic device can be split into three contributions ($\Delta E_{loss} = \Delta E_1 + \Delta E_2 + \Delta E_3$). The first term ΔE_1 is defined as the difference between the optical band gap and the highest possible free energy of photo-generated carriers under the Shockley-Queisser (SQ) model. The values of ΔE_1 mainly depend on the band gap of semiconductors and were determined to be 0.259, 0.263, and 0.268 eV for 0% LBL, 20% LBL, and 100% LBL devices, respectively. The second term ΔE_2 is additional radiative recombination loss, which originates from absorption of sub-gap states induced by energetic disorder. The 20% LBL and 100% LBL devices exhibit reduced
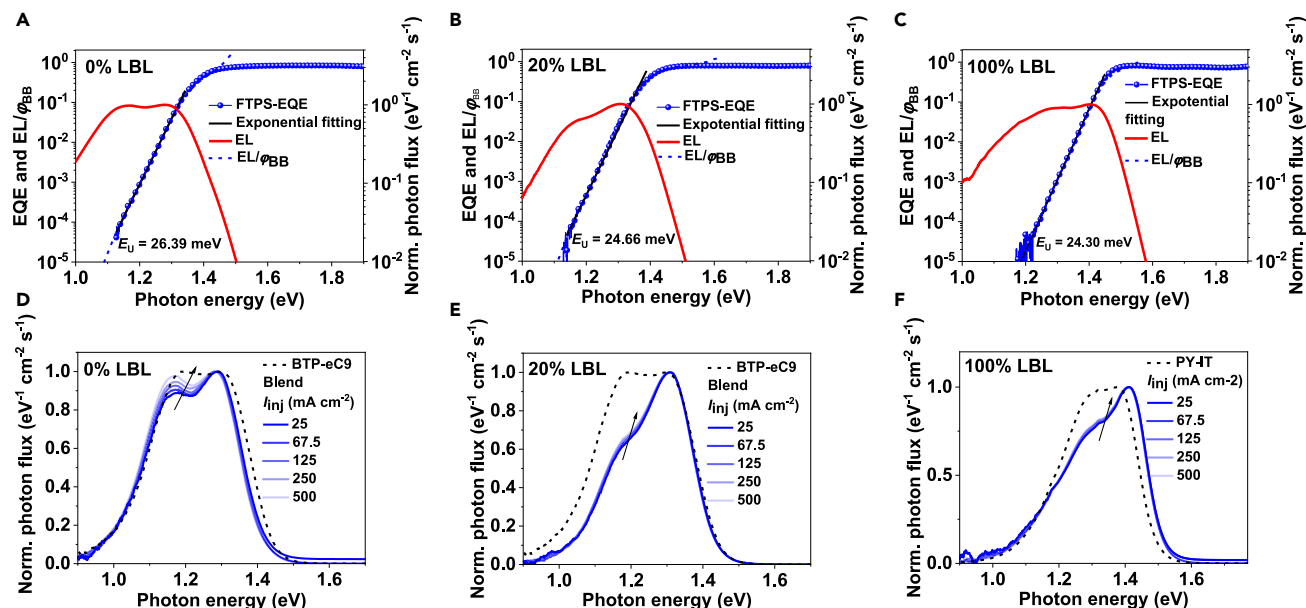
Figure 4. Energy loss analysis in three devices

(A–C) The measured EL spectrum (red solid line) and experimental EQE spectrum (blue dots) used to determine $V_{OC,Rad}$ for the (A) 0% LBL, (B) 20% LBL, and (C) 100% LBL devices. The dashed black line represents the deduced EQE spectrum determined from the EL spectrum via $\Phi_{EL}(E)/\varphi_{BB}(E)$, where $\varphi_{BB}(E)$ is the blackbody spectrum. The black solid line represents the best exponential fit to the Urbach rule.

(D–F) The EL spectra of devices at varied injected current densities for (D) 0% LBL, (E) 20% LBL, and (F) 100% LBL devices.

ΔE_2 of 0.059 and 0.042 eV, respectively, due to their relatively abrupt absorption edges. The last term ΔE_3 is non-radiative recombination loss and is scaled with the external radiative efficiency of EL (EQE_{EL}) of a photovoltaic device, following $\Delta E_3 = -k_B T ln(EQE_{EL})$. Here, k_B is the Boltzmann constant and T is the absolute temperature. The 0% LBL-based cell exhibited the EQE_{EL} value of 1.15×10^{-4}, corresponding to a ΔE_3 value of 0.236 eV. In comparison, the EQE_{EL} of the 20% LBL device was enhanced to 1.76×10^{-4} and the ΔE_3 was accordingly reduced to 0.225 eV. Noticeably, the 100% LBL-based cell exhibited the highest EQE_{EL} of 3.87×10^{-4} and the lowest ΔE_3 of 0.203 eV. Therefore, PY-IT is a low energy loss material with high EL quantum efficiency and suitable miscibility with the host A BTP-eC9 (Figure S3; Table S1), which contributes to the V_{OC} enhancement in ternary LBL-based devices.[42] The detailed three losses of LBL devices are summarized in Table S11.

On the one hand, the reduced ΔE_2 and ΔE_3 in 20% LBL device are attributed to the decreased energetic disorder in doped film, as evidenced by smaller values of Urbach energy E_U.[43,44] On the other hand, the wavefunction overlaps between the relaxed CT states and high-order vibrational modes of ground state decrease with the increment in CT energy, as illustrated in Figures 4D–4F. The rate constant of non-radiative recombination is significantly decreased, leading to enhanced values of EQE_{EL}, as predicted by the energy gap law.[45] Following the Urbach rule, $\alpha(E) = \alpha_0 e^{\frac{E-E_g}{E_U}}$, where α_0 is the optical absorption coefficient at the band edge, E is the photon energy, and E_U is the Urbach energy,[46,47] the 20% device delivers exceptionally lower energetic disorder with a determined E_U of 24.66 meV relative to that of 0% LBL film (E_U = 26.49 meV).

To get more insights into the relationship of electron transition and energetic disorder in amorphous films, the injected current-dependent EL measurement was

performed.[44] As shown in Figures 4D–4F, the CT emission peak in 0% LBL device is shifted toward higher energy for increased injected current densities. In contrast, the EL spectra of 20% LBL and 100% LBL devices are nearly independent of injected current densities. These different behaviors are associated with the degree of energetic disorder and can be interpreted by the spontaneous emission model.[48,49] The photon emission in a semiconductor is described by the convolution between occupied states in the conduction band and unoccupied states in the valence band. Compared with ordered systems, the central energies of the respective density of states (DOS) in disordered semiconductors increase in larger magnitude for a certain increment of quasi-Fermi level splitting. Therefore, a more apparent blue shift of the EL spectrum is observed in the 0% LBL device, whose degree of energetic disorder is the highest. To get deeper insights into the working mechanism, ultra-sensitive EQE (s-EQE) allows us to probe sub-gap features far below the CT state energy,[50–52] as shown in Figure S15. We note that the 100% LBL-type device shows negligible sub-gap absorption in the range of 0.8–1.0 eV, indicating almost absence of CT deep states in this OSC system.[53] For 20% LBL-type device, an obvious decrease in EQE response between 0.8 and 1.0 eV was observed relative to 0% LBL device, suggesting that trap-mediated loss pathways can be dramatically mitigated by p-i-n structure with reduced D-A heterojunctions. The CT deep traps can act as recombination centers presenting a trap-assisted recombination channel, thereby inhibiting CT deep trap states would reduce either radiative or non-radiative recombination losses and thus V_{OC} increase.[54]

Their corresponding BHJ counterparts are also studied, whose CT emission-dependent spectra can be found in Figure S16. Noticeably, the 20% BHJ-type device shows smaller E_U and lower ΔE_2 and ΔE_3 relative to the 0% BHJ device (summarized in Table S12), indicating that PY-IT can potentially inhibit trap states as a valid additional component. Furthermore, we notice that all three LBL-type devices exhibit lower E_U values than their BHJ counterparts, emphasizing the critical role of the GPT-LBL approach in lowering energetic disorder, thereby maximizing the three photovoltaic parameters of devices.

Morphology analysis

Atomic force microscopy (AFM) was employed to explore the surface aggregation properties at the top. As shown in Figure S17, the 20% and 100% LBL films show a smooth surface with small root-mean-square (RMS) values of 1.09 and 0.88 nm, respectively, whereas the 0% LBL film exhibited a rougher (RMS = 2.2 nm) surface. This may be due to the good film-processing properties of polymer material. In the phase images, 20% film shows clear fiber-like domains with appropriate size, which is closer to the top fibril feature in 100% LBL film, which could be assigned to the aggregation of polymeric PY-IT on the top. This observation coincides with the DP-XPS results. Two-dimensional (2D) grazing-incidence wide-angle X-ray scattering (GIWAXS) was employed to quantitatively investigate this molecular crystallinity of p-i-n structure induced by PY-IT, which is shown in Figures 5A–5D. To figure out PY-IT's role in tuning the molecular packing of BTP-eC9, we first evaluated the neat film GIWAXS results for neat BTP-eC9, PY-IT, and the mixed As (BTP-eC9:PY-IT), as shown in Figure S18. We can find that the neat BTP-eC9 and neat PY-IT films preferentially adopt the face-on orientation, supported by strong out-of-plane (OOP) π–π stacking diffractions (010) at 1.57 Å^{-1} (d= 4.00 Å), the in-plane (IP) lamellar (100) peak at 0.4 Å^{-1}, and OOP (010) at 1.72 Å^{-1} (d = 3.65 Å) and IP (100) at 0.4 Å^{-1}, respectively. For mixed As BTP-eC9:PY-IT, the IP lamellar peak and the OOP π-π stacking peak are observed at ~0.4 and 1.71Å^{-1} (d = 3.67Å), respectively, indicating that the addition of PY-IT does not change their face-on orientations and
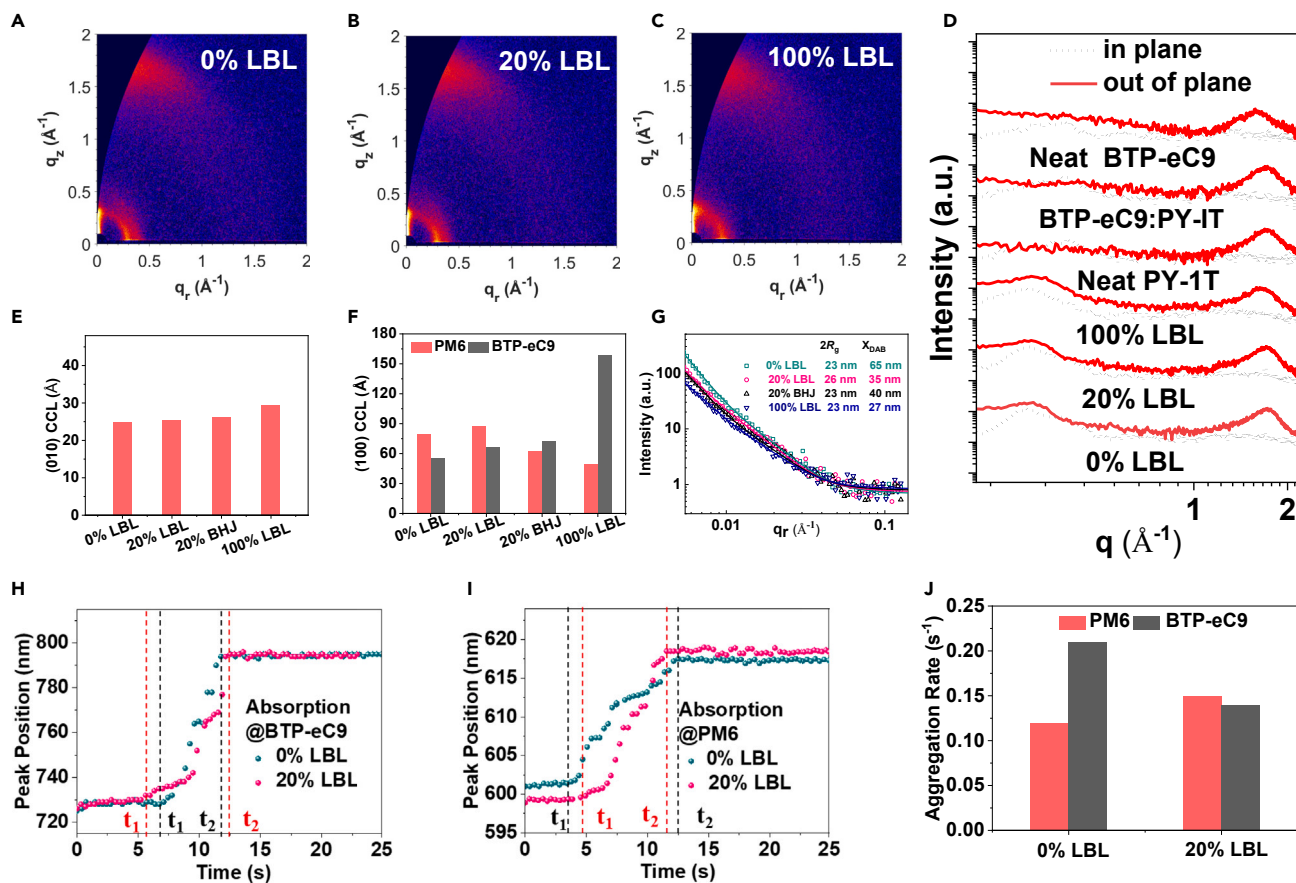
Figure 5. Morphological characterizations of relevant blends
(A–C) The 2D GIWAXS images of (A) 0% LBL, (B) 20% LBL, and (C) 100% LBL blends.
(D) The 1D X-ray profiles of the corresponding neat and LBL-based films.
(E) The CCL variations in OOP π-π stacking direction with an increase in PY-IT content in different films.
(F) The CCL variations in IP lamella direction for respective PM6 and BTP-eC9 with an increase in PY-IT content in different films.
(G) GISAXS intensity profiles and best fittings along the in-plane direction.
(H and I) The peak position evolution extracted from time-resolved UV-vis absorption spectra as a function of annealing time of (H) BTP-eC9 and (I) PM6 and in optimized 0% LBL and 20% LBL-type films.
(J) Aggregation rate of PM6 and BTP-eC9 in optimized 0% LBL and 20% LBL-type films.

can induce π–π molecular arrangement of As more compact. For the blended films (0%–100% LBL), they all showed a strong (010) π-π stacking peak along the OOP direction, originating from the overlapped PM6 and NFAs diffraction (Figures 5A–5D). The calculated parameters are summarized in Tables S13 and S14. In accordance with the Scherrer equation, 20% LBL and 20% BHJ blends both showed elongated coherence lengths (CCLs) along OOP (010) π-π stacking with 25.2 and 26.2 Å than 0% LBL (24.9 Å), which implies that the addition of PY-IT could enhance the intermolecular packings relative to the substrate. The fitting results can be found in Figure S19. The enlarged long-range ordering is favorable to the vertical charge transport in ternary devices, which agrees well with the enhanced FFs after adding PY-IT. In the IP direction, there are two distinct signals along the IP direction in the low-q regions one is at $q_{xy} \approx 0.3$ Å^{-1}, which should come from PM6, whereas the other is at $q_{xy} \approx 0.4$ Å^{-1}, which should be assigned to the NFAs with the contributions of both BTP-eC9 and PY-IT involved. This phenomenon allows for quantitively distinguishing the molecular packing and crystallization of individual PM6 and As by peak-fitting analysis (see Figure S20 for the details of the peak-fitting analysis). The

detailed parameters are summarized in Table S14 and Figures 5E and 5F. The binary blend showed that CCLs of the D and A along the IP (100) direction are 80.0 and 55.7 Å, respectively. Interestingly, the addition of PY-IT in the upper layer increased the A's crystal size (CCL= 66.3 Å) and the D's crystallites (CCL= 87.6 Å) and eventually achieved more balanced crystalline properties of D and A, which are in good match with their increased and balanced hole and electron mobilities as well as the improved photon utilizations. We also investigate the molecular packing of the ternary BHJ case for comparison. The different crystalline trend was found in 20% BHJ blends that PY-IT could enhance the crystallinity of BTP-eC9 (CCL = 72.7 Å) while decreasing the PM6's crystal size (62.8 Å); on the other hand, the 20% LBL blend could exhibit longer-range lamella ordering of PM6 (87.6 Å for 20% LB L and 62.8 Å for 20% BHJ;), which suggests that LBL approach tend to well maintain the microstructure of the underlying layer. Therefore, we can conclude that the PY-IT molecule assists the ordered arrangement of BTP-eC9 by synergistically promoting its OOP π-π stacking and IP lamella stacking and well-maintained crystalline PM6 domains for blends processed via two-step LBL method, promoting the ordered p-i-n microstructure formation and leading to higher FF.

Furthermore, we employed grazing-incidence small-angle X-ray scattering (GISAXS) to figure out the length scale of the phase separation in the blend films. Primitive patterns of the GISAXS results are provided in Figure S21, and the extracted line cuts of the fitted curves are shown in Figure 5G. For the 0% LBL blend, we can see that the calculated domain size for the pure A phase ($2R_g$) is 23 nm, and the intermixing phase (X_{DAB}) is 65 nm, suggesting efficient charge dissociation but potentially stronger charge recombination due to a more intermixed D/A phase. Then, the optimal 20% LBL film exhibited an increased A domain size with a length scale of 26 nm and an inhibited intermixed domain size with a length scale of 35 nm, contributing to a well-distributed film phase separation and thus more balanced charge transport and exciton dissociation. Compared with 20% LBL film, the effect of PY-IT on the morphology pattern of 20% BHJ blend film is primarily to manipulate the mixed D/A domains without altering the length scale of the crystalline A phase. These results indicate that the purer continuous A domains with better connectivity are more readily realized via sequential deposition engineering. Additionally, the smaller X_{DAB} for 100% LBL film is consistent with the poor miscibility between PY-IT and PM6.[55] Combined GISAXS and GIWAXS results, we can propose that the critical role of PY-IT in LBL-type film is to synergistically tune the mixed D/A phases and pure A phases. To be specific, the crystallization tendency of the material is enhanced, and in the meantime, the phase separation length scale is lessened. Benefiting from such reasonably optimal phase separation, exciton dissociation and charge transport are potentially balanced.

With the understanding of the GPT-LBL strategy-induced crystallinity enhancement of BTP-eC9 at the molecular level in mind, we further investigate the aggregation kinetics during LBL deposition processes, which can be probed by *in situ* time-resolved absorption spectroscopy (sketched in Figure S22). The evolution of absorption peak location represents the aggregation evolution of the D and the A. Generally, the whole film formation process can be divided into three stages. The first stage is the solvent vaporization stage, the second stage is the nucleation and crystal growth stage, and the third one is the final dried film stage. As shown in Figures 5H and 5I, during the first stage, the solvent evaporates, and the peak location of BTP-eC9 remains constant over time for both the 0% LBL film and 20% LBL film. As time goes on, the solvent evaporates slowly, and the solution reaches its solubility limit and then gets to nucleate. Under such extreme supersaturation, the BTP-eC9

CellPress

absorption peak starts to redshift, indicating the onset of the BTP-eC9 crystallization process. The peak location onset of BTP-eC9 in 20% LBL film (t_1 = ~5.24 s) redshifts much earlier than that in 0% LBL blend (t_1 = ~7.10 s), suggesting that PY-IT could promote earlier BTP-eC9 aggregation. As the solvent further evaporates, BTP-eC9 and PM6 absorption peaks continuously redshift and then remain unchanged when all the solvents are completely evaporated at the third stage. The slope of the peak can be used to indicate the aggregation rate, which is extracted in Figure 5J. Films fabricated at various PY-IT contents display different film-drying kinetic processes. In comparison with the 0% LBL film, the aggregation rate of PM6 increased from 0.12 to 0.15 s^{-1} for the 20% LBL film, whereas the aggregation rate of BTP-eC9 decreased from 0.21 to 0.14 s^{-1}, achieving more balanced crystallization kinetics between the D and the A. The aggregation rates for D and A of different LBL-OSCs are listed in Table S15. It is noted that the faster crystallization of PM6 can give the information that the swelling of the already-formed PM6 layer mainly in the amorphous regions without destroying the crystalline regions, making the crystalline PM6 regions convert to a solid state quickly from a semi-solution state.[17,20] Furthermore, the early liquid-liquid phase separation and slower aggregation of BTP-eC9 in the 20% LBL film allow sufficient time for small molecular nucleation and crystal formation, leading to more compact molecular packing and longer-range ordering of BTP-eC9 molecules,[56,57] which is in good accordance with GIWAXS and GISAXS results. Based on the aforementioned results, balanced crystallization kinetics between the D and the A and sufficient film formation time benefit an optimal morphology. To further figure out the underlying mechanism that PY-IT could regulate the film formation kinetics, the solution state is characterized to support the accurate kinetic process. Dynamic light scattering (DLS) measurements are employed to study the particle size distribution of two As in XY, indicative of the pre-aggregation size of small molecules in solution. As shown in Figure S24, the BTP-eC9 solution displays one Gaussian distribution of ~0.5 nm, and the DLS of the PY-IT solution shows a much larger sized distribution (~7 nm), which indicates that XY is a weaker solvent for PY-IT. Additionally, DLS shows a relatively increased size of ~2 nm in the A mixture compared with that of neat BTP-eC9, implying that the incorporation of PY-IT can strengthen the small molecular pre-aggregation behavior, which would induce the earlier crystallization of BTP-eC9.[57,58]

Combined with all the results discussed above, we have gained a whole morphological picture (Figure 6A) of how PY-IT induces the conceptual p-i-n structure and enables high crystallinity of BTP-eC9. PY-IT has a slightly poorer solubility than that of BTP-eC9 and turns to precipitate out earlier in the film-growth process, acting as a seed site to promote BTP-eC9 crystallization earlier.[13] This earlier molecular aggregation results in the dominant crystallization of BTP-eC9 on the top before it diffuses downward into the PM6 matrix, consequently leading to a rich A assembly at the top. In such a way, less swelling of the PM6 layer could almost reserve the compact packing of PM6 without disturbing the crystalline regions, thus promoting the classical p-i-n configuration. In addition, the extended film formation time would allow the A molecules to be assembled more sufficiently, thus facilitating the formation of good-quality crystallites with more compact molecular packing and ordered structure. As a result, a desired p-i-n vertical morphology with long-range ordered BTP-eC9 arrangement coupled with a purer domain was achieved.

Scalability and stability
Encouraged by the fact that the GPT-LBL strategy is effective in processing high-performance OSCs using non-halogenated solvent compatible with printing
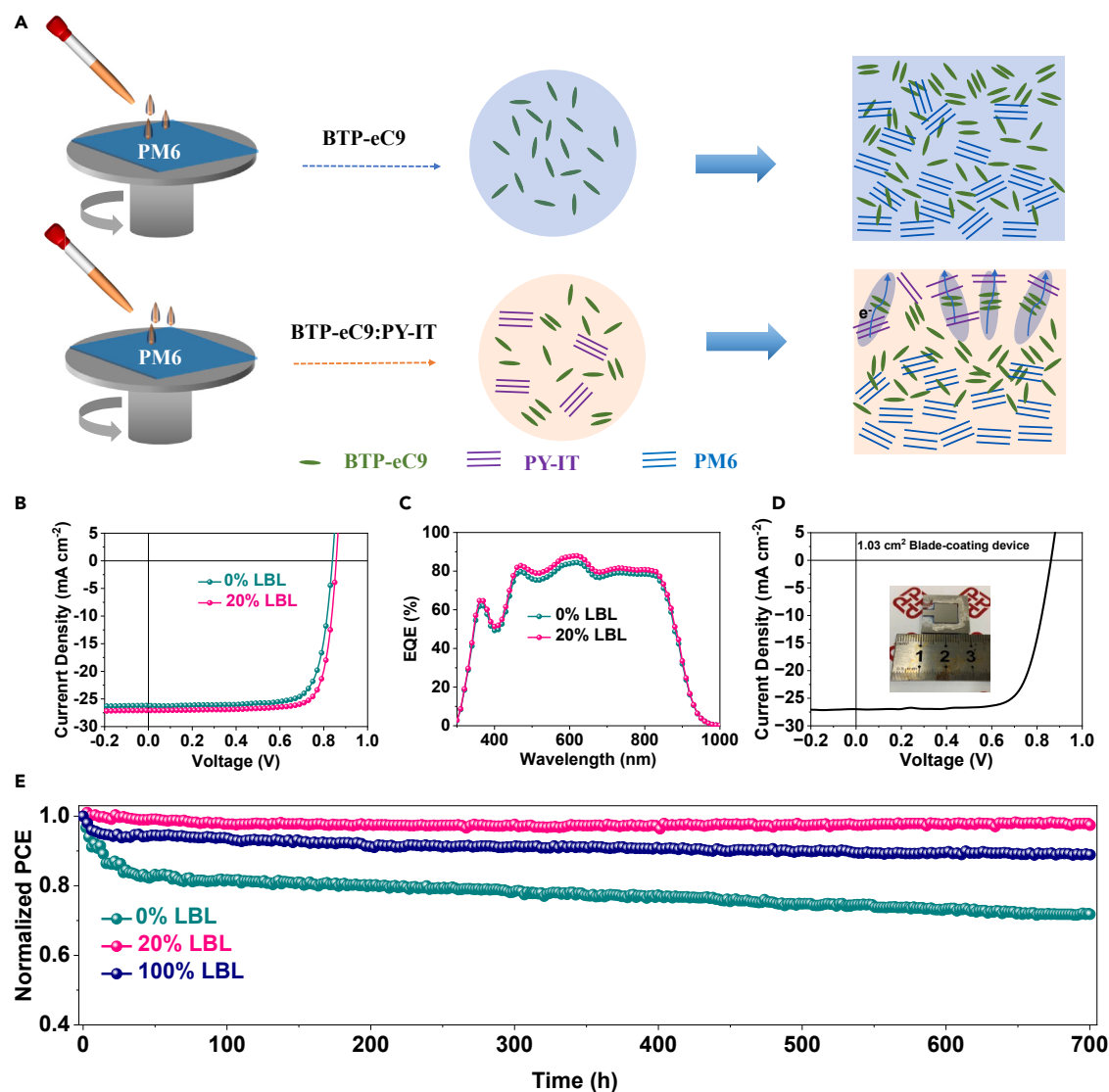
Figure 6. Schematic morphological illustration, scalability, and stability of optimal devices

(A) Schematic diagram of the crystallization process for 0% LBL and 20% LBL processed by XY.

(B) *J-V* curves of the blade-coated devices processed with a device area of 0.036 cm^2.

(C) EQE curves of the blade-coated devices processed with a device area of 0.036 cm^2.

(D) *J-V* curves of the blade-coated optimal 20% LBL device with an inset of a photograph of the 1.03 cm^2 blade-coated device.

(E) MPP tracking traces of encapsulated OSCs based on 0% and 20% LBL spin-coated devices in open atmosphere under the illumination of 100 mW cm^{-2}.

techniques, we transferred the spin-coating fabrication to doctor-blade coating. The fabrication details of the devices can be found in the supplemental information. As shown in Table S16 and Figure 6B, the open-air blade-coated device based on 20% LBL demonstrates an excellent PCE of 18.45%, outperforming that of 0% LBL-type device whose PCE is 17.03%. It is noted that we only blade-coated the active layer, and the interfacial layers are spin coated. These results show that the LBL bilayer structure optimization strategy is a truly potential candidate for gap minimization during lab-to-fab transferring. The EQE spectra of relevant devices are shown in Figure 6C. The 20% LBL device shows a high EQE, thus agreeing with the high J_{SC}. More importantly, non-halogenated high-boiling-point solvents also make it possible to

develop large-area devices; thus, we fabricated large-area OSC with the 20% LBL active layer by using XY as the processing solvent in ambient. Of note that upscaling device area may suffer from the increased sheet resistance of the conductive electrode (ITO), leading to unavoidable J_{SC} and FF losses.[15] As shown in Figure 6D and Table S16, the resulting 20% LBL large-area (1.03 cm^2) device provides an encouraging PCE of 17.52%, with a J_{SC} of 27.01 mA cm^{-2} and a well-maintained FF of 0.757. The inhibited trap states in the active layer with a superior p-i-n structure can promote the excellent up-scalable device performances of LBL cells.

In addition to the efficiency, device stability is also an indispensable factor for the practical application of OSCs. We further investigate the operational stability of the 0%, 20% LBL, and 100% LBL devices by exposing the corresponding encapsulated devices to continuous simulated 1-sun illumination under 100 mW cm^{-2} white LED with MPP tracking in ambient. Figure 6E displays the normalized PCEs as a function of aging time. It was found that the 0% LBL OSC suffered from a severe drop in PCE to 57% of its initial value after continuous illumination for 700 h, whereas the 100% LBL device retained 88% of its initial PCE after the same time aging. Impressively, the 20% LBL device maintained 96% of its initial PCE. We also observed a similarly enhanced stability trend in 20% BHJ devices under the same operational conditions (as shown in Figure S24). The results suggest that PY-IT has a positive influence on improving the long-term photostability of OSCs for both LBL- and BHJ-type OSCs. We corroborate such stability enhancements with the improved crystallinity of the active layer.[59]

To verify the role of the processing method (BHJ versus LBL) on the device stability, we extracted the photostability degradation curves of BHJ-type and LBL-type devices with varied contents of PY-IT for better comparison (Figure S25). It was observed that the LBL-processed devices exhibit better long-term light stability than BHJ-type devices. Here, we correlate the superior stability in LBL-type devices to (1) thermodynamically stable D-A network morphology formed by the spontaneous nanoscale phase separation[60] and (2) the preferable vertical phase separation with purer domains.[22] Therefore, the improved A domain connectivity with less isolated islands and more compact molecular packing after the addition of PY-IT could lock the film nanomorphology and prevent the small molecules from aggregation tendency upon exposure to the illumination.

Conclusions

In conclusion, a novel GPT-LBL strategy was used to constituent an optimal p-i-n microstructure with better vertical phase separation to achieve an outstanding PCE of 19.41% (certified 19.0%) with a very high FF of 0.813 processed by green solvents. The *in situ* and *ex situ* morphology analysis reveals that the delicate tuning of pre-aggregation kinetics of the upper layer is key to achieving graded morphology during LBL processing. Such favorable morphology was beneficial to the exciton dissociation, balanced charge transport, enhanced HT dynamics, mitigated energy loss, trap state densities, and thus PCE increment of OSCs. More importantly, the GPT-LBL strategy-enabled p-i-n microstructure with superior carrier behaviors shows great potential in fabricating highly efficient blade-coating OSCs in open air, facilitating small area (0.036 cm^2) and large area (1.03 cm^2) to deliver satisfactory PCEs of 18.45% and 17.52%, respectively. Therefore, our work provides new insights into the optimization method in the LBL-processing technique and establishes the close correlation among processing-microstructure-photophysical properties performances, enabling efficient, stable, and scalable OSCs and promoting the future commercialization for the OSC field.

🌱 **CellPress**

Joule
Article

EXPERIMENTAL PROCEDURES
Resource availability
Lead contact
Further information and requests for resources and materials should be directed to and will be fulfilled by the lead contact, Gang Li (gang.w.li@polyu.edu.hk).

Materials availability
This study did not generate new unique materials.

Data and code availability
All data are present in the paper and supplemental information. Other data are available from the lead contact or corresponding author.

Full details of experimental procedures can be found in the supplemental information.

SUPPLEMENTAL INFORMATION
Supplemental information can be found online at https://doi.org/10.1016/j.joule.2023.12.009.

AUTHOR CONTRIBUTIONS
Y.Z. and G.L. conceived and Y.Y. refined the idea. Y.Z. and Y.L. performed the device fabrication experiments, characterizations, and formal data analysis. W.D. and H.W. conducted the EL and FTPS-EQE measurement and analyzed the data. C.E.P., H.T., and F.L. conducted TAS characterizations and did the data analysis. X.X. and X.L. conducted the GIWAXS and GISAXS characterizations. H.X. and K.L. conducted contact angle and AFM measurements. H.T.C., S.M., and S.-W.T. conducted the s-EQE characterizations. P.W.K.F conducted *in situ* absorption measurement. Y.L. and J.W. conducted the TOF-SIMS characterizations. Y.Z. wrote the original draft manuscript. G.L., Y.Z., and Y.Y. designed the experiments and methodology and revised the manuscript. All authors discussed and commented on the key scientific issues in the work.

DECLARATION OF INTERESTS
The authors declare no competing interests.

Joule
Article

CellPress

REFERENCES

1. Li, G., Zhu, R., and Yang, Y. (2012). Polymer solar cells. Nat. Photonics 6, 153–161.

2. Zhao, Y., Zhu, Y., Cheng, H.-W., Zheng, R., Meng, D., and Yang, Y. (2021). A review on semitransparent solar cells for agricultural application. Mater. Today Energy 22, 100852.

3. Cheng, P., Li, G., Zhan, X., and Yang, Y. (2018). Next-generation organic photovoltaics based on non-fullerene acceptors. Nat. Photonics 12, 131–142.

4. Hou, J., Inganäs, O., Friend, R.H., and Gao, F. (2018). Organic solar cells based on non-fullerene acceptors. Nat. Mater. 17, 119–128.

5. Zhang, J., Tan, H.S., Guo, X., Facchetti, A., and Yan, H. (2018). Material insights and challenges for non-fullerene organic solar cells based on small molecular acceptors. Nat. Energy 3, 720–731.

6. Fu, J., Fong, P.W.K., Liu, H., Huang, C.-S., Lu, X., Lu, S., Abdelsamie, M., Kodalle, T., Sutter-Fella, C.M., Yang, Y., et al. (2023). 19.31% binary organic solar cell and low non-radiative recombination enabled by non-monotonic intermediate state transition. Nat. Commun. 14, 1760.

7. Yuan, J., Zhang, Y., Zhou, L., Zhang, G., Yip, H.-L., Lau, T.-K., Lu, X., Zhu, C., Peng, H., Johnson, P.A., et al. (2019). Single-junction organic solar cell with over 15% efficiency using fused-ring acceptor with electron-deficient core. Joule 3, 1140–1151.

8. Cui, Y., Xu, Y., Yao, H., Bi, P., Hong, L., Zhang, J., Zu, Y., Zhang, T., Qin, J., Ren, J., et al. (2021). Single-junction organic photovoltaic cell with 19% efficiency. Adv. Mater. 33, e2102420.

9. Liu, T., Yang, T., Ma, R., Zhan, L., Luo, Z., Zhang, G., Li, Y., Gao, K., Xiao, Y., Yu, J., et al. (2021). 16% efficiency all-polymer organic solar cells enabled by a finely tuned morphology via the design of ternary blend. Joule 5, 914–930.

10. Bi, P., Zhang, S., Chen, Z., Xu, Y., Cui, Y., Zhang, T., Ren, J., Qin, J., Hong, L., Hao, X., et al. (2021). Reduced non-radiative charge recombination enables organic photovoltaic cell approaching 19% efficiency. Joule 5, 2408–2419.

11. Ma, R., Yan, C., Yu, J., Liu, T., Liu, H., Li, Y., Chen, J., Luo, Z., Tang, B., Lu, X., et al. (2022). High-efficiency ternary organic solar cells with a good figure-of-merit enabled by two low-cost donor polymers. ACS Energy Lett. 7, 2547–2556.

12. Zhan, L., Yin, S., Li, Y., Li, S., Chen, T., Sun, R., Min, J., Zhou, G., Zhu, H., Chen, Y., et al. (2022). Multiphase morphology with enhanced carrier lifetime via quaternary strategy enables high-efficiency thick-film and large-area organic photovoltaics. Adv. Mater. 34, 2206269.

13. Zhu, L., Zhang, M., Xu, J., Li, C., Yan, J., Zhou, G., Zhong, W., Hao, T., Song, J., Xue, X., et al. (2022). Single-junction organic solar cells with over 19% efficiency enabled by a refined double-fibril network morphology. Nat. Mater. 21, 656–663.

14. Li, G., Shrotriya, V., Huang, J., Yao, Y., Moriarty, T., Emery, K., and Yang, Y. (2005). High-efficiency solution processable polymer photovoltaic cells by self-organization of polymer blends. Nat. Mater. 4, 864–868.

15. Zhang, Y., Lang, Y., and Li, G. (2023). Recent advances of non-fullerene organic solar cells: from materials and morphology to devices and applications. Ecomat. 5, 12281.

16. Yu, G., Gao, J., Hummelen, J.C., Wudl, F., and Heeger, A.J. (1995). Polymer photovoltaic cells: enhanced efficiencies via a network of internal donor-acceptor heterojunctions. Science 270, 1789–1791.

17. Zhan, L., Li, S., Xia, X., Li, Y., Lu, X., Zuo, L., Shi, M., and Chen, H. (2021). Layer-by-layer processed ternary organic photovoltaics with efficiency over 18. Adv. Mater. 33, e2007231.

18. Sun, R., Wang, T., Yang, X., Wu, Y., Wang, Y., Wu, Q., Zhang, M., Brabec, C.J., Li, Y., and Min, J. (2022). High-speed sequential deposition of photoactive layers for organic solar cell manufacturing. Nat. Energy 7, 1087–1099.

19. Hong, L., Yao, H., Cui, Y., Bi, P., Zhang, T., Cheng, Y., Zu, Y., Qin, J., Yu, R., Ge, Z., et al. (2021). 18.5% efficiency organic solar cells with a hybrid planar/bulk heterojunction. Adv. Mater. 33, e2103091.

20. Zhang, Y., Liu, K., Huang, J., Xia, X., Cao, J., Zhao, G., Fong, P.W.K., Zhu, Y., Yan, F., Yang, Y., et al. (2021). Graded bulk-heterojunction enables 17% binary organic solar cells via nonhalogenated open air coating. Nat. Commun. 12, 4815.

21. Dong, S., Zhang, K., Xie, B., Xiao, J., Yip, H.-L., Yan, H., Huang, F., and Cao, Y. (2019). High-performance large-area organic solar cells enabled by sequential bilayer processing via nonhalogenated solvents. Adv. Energy Mater. 9, 1802832.

22. Sun, R., Guo, J., Wu, Q., Zhang, Z., Yang, W., Guo, J., Shi, M., Zhang, Y., Kahmann, S., Ye, L., et al. (2019). A multi-objective optimization-based layer-by-layer blade-coating approach for organic solar cells: rational control of vertical stratification for high performance. Energy Environ. Sci. 12, 3118–3132.

23. Gevaerts, V.S., Koster, L.J., Wienk, M.M., and Janssen, R.A. (2011). Discriminating between bilayer and bulk heterojunction polymer:fullerene solar cells using the external quantum efficiency. ACS Appl. Mater. Interfaces 3, 3252–3255.

24. Sun, R., Wu, Q., Guo, J., Wang, T., Wu, Y., Qiu, B., Luo, Z., Yang, W., Hu, Z., Guo, J., et al. (2020). A layer-by-layer architecture for printable organic solar cells overcoming the scaling lag of module efficiency. Joule 4, 407–419.

25. Zheng, Y., Sun, R., Zhang, M., Chen, Z., Peng, Z., Wu, Q., Yuan, X., Yu, Y., Wang, T., Wu, Y., et al. (2021). Baseplate temperature-dependent vertical composition gradient in pseudo-bilayer films for printing non-fullerene organic solar cells. Adv. Energy Mater. 11, 2102135.

26. Du, X., Heumueller, T., Gruber, W., Almora, O., Classen, A., Qu, J., He, F., Unruh, T., Li, N., and Brabec, C.J. (2020). Unraveling the microstructure-related device stability for polymer solar cells based on nonfullerene small-molecular acceptors. Adv. Mater. 32, e1908305.

27. Zhu, Y., Gadisa, A., Peng, Z., Ghasemi, M., Ye, L., Xu, Z., Zhao, S., and Ade, H. (2019). Rational strategy to stabilize an unstable high-efficiency binary nonfullerene organic solar cells with a third component. Adv. Energy Mater. 9, 1900376.

28. van Franeker, J.J., Kouijzer, S., Lou, X., Turbiez, M., Wienk, M.M., and Janssen, R.A.J. (2015). Depositing fullerenes in swollen polymer layers via sequential processing of organic solar cells. Adv. Energy Mater. 5, 1500464.

29. Zhang, G., Huber, R.C., Ferreira, A.S., Boyd, S.D., Luscombe, C.K., Tolbert, S.H., and Schwartz, B.J. (2014). Crystallinity effects in sequentially processed and blend-cast bulk-heterojunction polymer/fullerene photovoltaics. J. Phys. Chem. C 118, 18424–18435.

30. Cui, Y., Zhang, S., Liang, N., Kong, J., Yang, C., Yao, H., Ma, L., and Hou, J. (2018). Toward efficient polymer solar cells processed by a solution-processed layer-by-layer approach. Adv. Mater. 30, e1802499.

31. Ye, L., Xiong, Y., Chen, Z., Zhang, Q., Fei, Z., Henry, R., Heeney, M., O'Connor, B.T., You, W., and Ade, H. (2019). Sequential deposition of organic films with eco-compatible solvents improves performance and enables over 12%-efficiency nonfullerene solar cells. Adv. Mater. 31, e1808153.

32. Arunagiri, L., Zhang, G., Hu, H., Yao, H., Zhang, K., Li, Y., Chow, P.C.Y., Ade, H., and Yan, H. (2019). Temperature-dependent aggregation donor polymers enable highly efficient sequentially processed organic photovoltaics without the need of orthogonal solvents. Adv. Funct. Mater. 29, 1902478.

33. Baran, D., Ashraf, R.S., Hanifi, D.A., Abdelsamie, M., Gasparini, N., Röhr, J.A., Holliday, S., Wadsworth, A., Lockett, S., Neophytou, M., et al. (2017). Reducing the efficiency-stability-cost gap of organic photovoltaics with highly efficient and stable small molecule acceptor ternary solar cells. Nat. Mater. 16, 363–369.

34. Bi, P., Wang, J., Cui, Y., Zhang, J., Zhang, T., Chen, Z., Qiao, J., Dai, J., Zhang, S., Hao, X., et al. (2023). Enhancing photon utilization efficiency for high-performance organic photovoltaic cells via regulating phase-transition kinetics. Adv. Mater. 35, e2210865.

35. Wang, Y., Zhu, Q., Naveed, H.B., Zhao, H., Zhou, K., and Ma, W. (2020). Sequential blade-coated acceptor and donor enables simultaneous enhancement of efficiency, stability, and mechanical properties for organic solar cells. Adv. Energy Mater. 10, 1903609.

36. Yang, W., Luo, Z., Sun, R., Guo, J., Wang, T., Wu, Y., Wang, W., Guo, J., Wu, Q., Shi, M., et al. (2020). Simultaneous enhanced efficiency and thermal stability in organic solar cells from a polymer acceptor additive. Nat. Commun. 11, 1218.

CellPress

Joule
Article

37. Hedley, G.J., Ruseckas, A., and Samuel, I.D. (2017). Light harvesting for organic photovoltaics. Chem. Rev. *117*, 796–837.

38. Comyn, J. (1992). Contact angles and adhesive bonding. Int. J. Adhes. Adhes. *12*, 145–149.

39. Fu, H., Gao, W., Li, Y., Lin, F., Wu, X., Son, J.H., Luo, J., Woo, H.Y., Zhu, Z., and Jen, A.K.-Y. (2020). A generally applicable approach using sequential deposition to enable highly efficient organic solar cells. Small Methods *4*, 2000687.

40. Juška, G., Arlauskas, K., Viliūnas, M., and Kočka, J. (2000). Extraction current transients: new method of study of charge transport in microcrystalline silicon. Phys. Rev. Lett. *84*, 4946–4949.

41. Karuthedath, S., Gorenflot, J., Firdaus, Y., Chaturvedi, N., De Castro, C.S.P., Harrison, G.T., Khan, J.I., Markina, A., Balawi, A.H., Peña, T.A.D., et al. (2021). Intrinsic efficiency limits in low-bandgap non-fullerene acceptor organic solar cells. Nat. Mater. *20*, 378–384.

42. Wang, Y., Yu, J., Zhang, R., Yuan, J., Hultmark, S., Johnson, C.E., Gallop, N.P., Siegmund, B., Qian, D., Zhang, H., et al. (2023). Origins of the open-circuit voltage in ternary organic solar cells and design rules for minimized voltage losses. Nat. Energy *8*, 978–988.

43. Zhang, Z., Li, Y., Cai, G., Zhang, Y., Lu, X., and Lin, Y. (2020). Selenium heterocyclic electron acceptor with small Urbach energy for as-cast high-performance organic solar cells. J. Am. Chem. Soc. *142*, 18741–18745.

44. Liu, S., Yuan, J., Deng, W., Luo, M., Xie, Y., Liang, Q., Zou, Y., He, Z., Wu, H., and Cao, Y. (2020). High-efficiency organic solar cells with low non-radiative recombination loss and low energetic disorder. Nat. Photonics *14*, 300–305.

45. Azzouzi, M., Yan, J., Kirchartz, T., Liu, K., Wang, J., Wu, H., and Nelson, J. (2018). Nonradiative energy losses in bulk-heterojunction organic photovoltaics. Phys. Rev. X *8*, 31055.

46. Vandewal, K., Tvingstedt, K., Gadisa, A., Inganäs, O., and Manca, J.V. (2010). Relating the open-circuit voltage to interface molecular properties of donor:acceptor bulk heterojunction solar cells. Phys. Rev. B *81*, 125204.

47. Kaiser, C., Sandberg, O.J., Zarrabi, N., Li, W., Meredith, P., and Armin, A. (2021). A universal Urbach rule for disordered organic semiconductors. Nat. Commun. *12*, 3988.

48. Gong, W., Faist, M.A., Ekins-Daukes, N.J., Xu, Z., Bradley, D.D.C., Nelson, J., and Kirchartz, T. (2012). Influence of energetic disorder on electroluminescence emission in polymer:fullerene solar cells. Phys. Rev. B *86*, 24201.

49. Deng, W., Liu, W., Qian, R., and Wu, H. (2022). Toward high-efficiency organic photovoltaics: perspectives on the origin and role of energetic disorder. J. Phys. Chem. Lett. *13*, 544–551.

50. Street, R.A., Northrup, J.E., and Krusor, B.S. (2012). Radiation induced recombination centers in organic solar cells. Phys. Rev. B *85*, 205211.

51. Dou, L., You, J., Hong, Z., Xu, Z., Li, G., Street, R.A., and Yang, Y. (2013). 25th anniversary article: a decade of organic/polymeric photovoltaic research. Adv. Mater. *25*, 6642–6671.

52. Thachoth Chandran, H., Tang, H., Liu, T., Mahadevan, S., Liu, K., Lu, Z., Huang, J., Ren, Z., Liao, F., Chai, Y., et al. (2023). Architecturally simple organic photodiodes with highly competitive figures of merit via a facile self-assembly strategy. Mater. Horiz. *10*, 918–927.

53. Street, R.A., Krakaris, A., and Cowan, S.R. (2012). Recombination through different types of localized states in organic solar cells. Adv. Funct. Mater. *22*, 4608–4619.

54. Zarrabi, N., Sandberg, O.J., Zeiske, S., Li, W., Riley, D.B., Meredith, P., and Armin, A. (2020). Charge-generating mid-gap trap states define the thermodynamic limit of organic photovoltaic devices. Nat. Commun. *11*, 5567.

55. Naveed, H.B., and Ma, W. (2018). Miscibility-driven optimization of nanostructures in ternary organic solar cells using non-fullerene acceptors. Joule *2*, 621–641.

56. Chen, H., Zhang, R., Chen, X., Zeng, G., Kobera, L., Abbrent, S., Zhang, B., Chen, W., Xu, G., Oh, J., et al. (2021). A guest-assisted molecular-organization approach for >17% efficiency organic solar cells using environmentally friendly solvents. Nat. Energy *6*, 1045–1053.

57. Lin, B., Zhou, X., Zhao, H., Yuan, J., Zhou, K., Chen, K., Wu, H., Guo, R., Scheel, M.A., Chumakov, A., et al. (2020). Balancing the pre-aggregation and crystallization kinetics enables high efficiency slot-die coated organic solar cells with reduced non-radiative recombination losses. Energy Environ. Sci. *13*, 2467–2479.

58. Liu, Y., Zhao, J., Li, Z., Mu, C., Ma, W., Hu, H., Jiang, K., Lin, H., Ade, H., and Yan, H. (2014). Aggregation and morphology control enables multiple cases of high-efficiency polymer solar cells. Nat. Commun. *5*, 5293.

59. Nam, M., Cha, M., Lee, H.H., Hur, K., Lee, K.T., Yoo, J., Han, I.K., Kwon, S.J., and Ko, D.H. (2017). Long-term efficient organic photovoltaics based on quaternary bulk heterojunctions. Nat. Commun. *8*, 14068.

60. Yu, R., Wei, X., Wu, G., and Tan, Z. (2022). Layer-by-layered organic solar cells: morphology optimizing strategies and processing techniques. Aggregate *3*, 107.